Available online at www.sciencedirect.com
SCIENCE DIRECT®
International Journal of Heat and Mass Transfer 47 (2004) 3745–3756
International Journal of HEAT and MASS TRANSFER
www.elsevier.com/locate/ijhmt

A study on the performance of the airside heat exchanger under frosting in an air source heat pump water heater/chiller unit

Yang Yao [a], Yiqiang Jiang [a,b], Shiming Deng [b,*], Zuiliang Ma [a]

[a] *Harbin Institute of Technology, Harbin, China*
[b] *Department of Building Service Engineering, The Hong Kong Polytechnic University, Kowloon, Hong Kong SAR, China*

Received 5 June 2003; received in revised form 19 March 2004
Available online 6 May 2004

Abstract

Air source heat pump water heater/chiller (ASHPWHC) units, a cooling and heating source for buildings becomes increasingly popular. However, when such a unit is operated as a heating source under low ambient temperature in winter, the formation of frost on the surface of its airside heat exchanger becomes problematic, leading to the degradation of the heat exchanger's performance or even the shutdown of a unit. Therefore it is necessary to have a detailed investigation on the operational characteristic of the airside heat exchanger in an ASHPWHC unit under frosting in order to optimize its structural layout, thus increasing its energy efficiency and operational reliability.

This paper first reports on the development of a distributed mathematical model of the airside heat exchanger under frosting in an ASHPWHC unit. The model, firstly seen in open literature, consists of a frosting sub-model and a heat exchanger sub-model. This is followed by an evaluation of operational characteristics of the airside heat exchanger under frosting in an ASHPWHC unit using the model developed. In addition, the impacts of frosting on the operational performance of an ASHPWHC unit were also evaluated. The discussions of optimizing the structural layout of finned tubes used in an airside heat exchanger and improving defrosting control measures are also included in analyzing the simulated results.

Keywords: Air source heat pump; Frosting; Distributed modeling; Performance evaluation; Operational characteristics

1. Introduction

Air source heat pump water heater/chiller (ASHPWHC) units, a cooling and heating source for building heating, ventilation and air conditioning (HVAC) systems, becomes increasingly popular. For example, currently, there are many ASHPWAC units, compared to some years ago only a few, being used in commercial districts in major cities in China [1]. However, when such a unit is operated as a heating source under low ambient temperature in winter, the formation of frost on the surface of its airside heat exchanger becomes problematic, leading to the degradation of the heat exchanger's performance. These include lower heat transfer efficiency, a higher airside pressure drop and a reduced heating capacity. The formation of frost may sometimes even cause the shutdown of a unit. Therefore it is necessary to have a detailed investigation on the characteristic of the airside heat exchanger in an ASHPWHC unit under frosting in order to optimize its structural layout, thus increasing its energy efficiency and operational reliability.

Currently, a substantial amount of literature is available on frost properties and growth [2–4]. A large number of experimental and theoretical investigations on frost properties, the mechanism of frost growth, and

* Corresponding author. Tel.: +852-2766-5859; fax: +852-2765-7198.
E-mail address: besmd@polyu.edu.hk (S. Deng).

0017-9310/$ - see front matter © 2004 Elsevier Ltd. All rights reserved.
doi:10.1016/j.ijheatmasstransfer.2004.03.013

Nomenclature

A	area (m^2)
a	constant/coefficient
D	diameter of pipe (m)
d	moisture content (kg water vapor kg^{-1} dry air)
D_s	diffusivity of water vapor in air ($m^2\,s^{-1}$)
F	friction ($N\,m^{-1}$)
f	friction coefficient
h	enthalpy ($kJ\,kg^{-1}$)
L	fin height (m)
M	mass
m	parameter defined by Eq. (31)
$\dot{m}$	mass flow/accumulation rate ($kg\,s^{-1}$)
n	number of row/element
p	pressure (Pa)
Pr	Prandtl number
Q	overall energy transfer (W)
$\dot{q}$	heat flux ($W\,m^{-2}$)
R	gas constant of water vapor
Re	Reynolds number
S	distance (m)
Sc	Schmidt number
T	temperature (°C or K)
t	time (s)
u	velocity (ms^{-1})
v	specific volume ($m^3\,kg^{-1}$)
$\dot{w}$	water vapor flux ($kgm^{-2}\,s^{-1}$)
X_{tt}	Lockhart–Martinelli parameter
x	dryness fraction/coordinate
z	coordinate

Greek symbols

λ	thermal conductivity ($W\,m^{-1}\,K^{-1}$)
δ	thickness/height (mm)
α	heat transfer coefficient ($W\,m^{-2}\,K^{-1}$)
$\bar{\alpha}$	void faction
μ	dynamic viscosity (Pa s)
Δ	difference
ρ	density ($kg\,m^{-3}$)
v	kinematic viscosity ($m^2\,s^{-1}$)

Subscripts

a	air
d	dry-out
e	evaporation
f	fin
fr	frost
i	ice/inside/inlet
L	liquid phase
min	minimum
o	outlet
p	pressure, pipe
PW	pipe wall
r	refrigerant
S	surface
Sb	sublimation of water vapor
Sp	superheat
St	saturation water vapor
t	total
tp	two phases
V	vapor
ρ	density
δ	thickness/height

the heat transfer involved in frost growth have been performed and reported for simple geometry heat exchangers, such as tubule [5], annuli [6], cylinders [7,8], flat plates and parallel plates [9–11]. However, for heat exchangers with a more complex geometry, such as a finned tube heat exchanger, the amount of literature available is limited. The reasons for this may include the very large number of variables involved, the complex surface geometry of heat exchangers and the thermodynamic properties of humid air and frost. Kondepudi and O'Neal [12] reviewed the available literature on the effects of frost formation and growth on finned tube heat exchanger performance. Senshu and Yasdua [13,14] predicted the performance of a cross-finned tube heat exchanger on which frost occurred using a mathematical model. However, since this model was built based on the experimental data from only one type of heat exchanger, its use cannot be generally extended to other types of heat exchangers. Oskarsson and Krakow [15,16] showed a finite model, a three-region model and a parameter model for finned evaporator in dry, wet, and frosted finned surface conditions, respectively. However, it was assumed in these models that the heat transfer coefficients for both a wet and a frosted coil surface were the same as that for a dry coil surface. This does not appear physically meaningful. Furthermore, previous reported experimental studies on performance evaluation for the finned tube heat exchanger in an ASHPWHC unit under frosting are not available in open literature. There has been a lack of detailed models for analyzing frost growth on finned tube heat exchangers which are in fact widely used in ASHPWHC units. Therefore the performance evaluation of airside heat exchangers under frosting by using detailed model simulation has been limited.

This paper first reports on the development of a detailed distributed model for the airside heat exchanger under frosting in an ASHPWHC unit. The distributed model developed, firstly seen in open literature, consists of a frosting sub-model and a heat exchanger sub-model. This is followed by reporting an evaluation of the operational characteristics of a frosted airside heat exchanger in an ASHPWHC unit under different ambient conditions using the model developed. These include frost formation and its distribution on the surface of the airside heat exchanger, and their impacts on the operational performance of an ASHPWHC unit. Based on the evaluation, the optimization of structural layout for finned tubes used in an airside heat exchanger and the measures for improving defrosting control so as to increase the energy efficiency and operational reliability of an ASHPWHC unit, are also discussed.

2. Model development

The model of can be divided into two sub-models, i.e., a frosting sub-model and a heat exchanger sub-model which consists of three modules for refrigerant side, pipe wall and air side, respectively.

In developing the model, the following assumptions have been made:

(1) Refrigerant in both liquid and gas phase is considered incompressible and in a thermal equilibrium.
(2) Refrigerant flows in one dimension along the heat exchanger pipe axis.
(3) In the two-phase flow region at any cross-section perpendicular to refrigerant flow direction, the pressure of liquid refrigerant equals to that of gas refrigerant.
(4) Both kinetic energy and potential energy are neglected in energy conservation equation.
(5) The heat transfer by radiation between the moist air and frost is negligible.
(6) The problem of frosting is assumed to be of the nature of quasi-steady-state.
(7) Frost is formed layer by layer. The density and thermal conductivity of each frost layer are entirely dependent on the interface temperature between air and frost.
(8) A linear relationship between saturated air enthalpy and air dry bulb temperature is assumed, with air temperature ranging from −25 to 20 °C, i.e., $h_a = a + a_1 t_a$.

3. The frosting sub-model

The frost accumulation rate is determined by a loss of water vapor in the air, as water vapor condenses on the cold coil surface of an airside heat exchanger. It is expressed by

$$\dot{m}_{fr} = \dot{m}_a(d_i - d_o) \tag{1}$$

Based on the physical change of frost in term of both density and thickness, Eq. (1) can be rewritten as:

$$\dot{m}_{fr} = \dot{m}_a(d_i - d_o) = \frac{d}{dt}(\delta_S \rho_{fr}) = \rho_{fr}\frac{d\delta_S}{dt} + \delta_S \frac{d\rho_{fr}}{dt} \tag{2}$$

where δ_S and ρ_{fr} denote frost thickness and density, respectively. By this arrangement, the total amount of water vapor approaching a frost layer for solidification is now separated into two terms. The first term $(\rho_{fr}\frac{d\delta_S}{dt})$ represents the amount of water vapor condensed contributing to the increase of frost thickness, and the second term $(\delta_S \frac{d\rho_{fr}}{dt})$ to the increase of frost density. Therefore, the total mass flux can be given as

$$\dot{m}_{fr} = \dot{m}_\delta + \dot{m}_\rho \tag{3}$$

Kondepudi and O'Neal [17] used the following expression for the mass of water vapor diffusing through a porous frost layer:

$$\dot{m}_\rho = A_t D_S \left[\frac{1 - (\rho_{fr}/\rho_i)}{1 + (\rho_{fr}/\rho_i)^{0.5}}\right]\frac{d\rho_V}{dx} \tag{4}$$

An empirical equation for the molecular diffusivity by Ecker and Drake [18], used largely for water vapor in a frosting process, was followed in the current study

$$D_S = 2.302(0.98 \times 10^5/p_a)(T_S/256)^{1.81} \times 10^{-5} \tag{5}$$

The water vapor on a frost surface can be described by the ideal gas state equation ($p_V = \rho_V R T_S$) because of its substantially low partial pressure of water vapor (p_V). The following equation can therefore be derived:

$$\frac{d\rho_V}{dx} = \frac{1}{RT_S}\left(\frac{dp_V}{dT_S} - \frac{p_V}{T_S}\right)\frac{dT_S}{dx} \tag{6}$$

The Clapeyron–Clausius equation is

$$\frac{dp_V}{dT_S} = \frac{h_{Sb}}{T_S(v_V - v_i)} \tag{7}$$

Substituting Eqs. (6) and (7) into Eq. (4) results in

$$\dot{m}_\rho = A_t D_S \left[\frac{1 - (\rho_{fr}/\rho_i)}{1 + (\rho_{fr}/\rho_i)^{0.5}}\right]\left(\frac{1}{RT_S}\right) \times \left[\frac{h_{Sb}}{T_S(v_V - v_i)} - \frac{p_V}{T_S}\right]\frac{dT_S}{dx} \tag{8}$$

On the other hand, the total energy transferred to the frost layer includes sensible heat transferred from air and the latent heat of solidification released by water vapor as it diffuses into the frost layer and solidifies. That is

$$\dot{Q}_t = A_t \lambda_{fr}\frac{dT_S}{dx} + \dot{m}_\rho h_{Sb} \tag{9}$$

Combining Eqs. (8) and (9) yields

$$\dot{m}_\rho = \frac{\dot{Q}_t}{h_{Sb} + \dfrac{\lambda_{fr} R T_S^2 (v_V - v_i)}{D_S[h_{Sb} - p_V(v_V - v_i)]\left(1 - \frac{\rho_{fr}}{\rho_i}\right) \Big/ \left[1 + \left(\frac{\rho_{fr}}{\rho_i}\right)^{0.5}\right]}} \tag{10}$$

The frost density, ρ_{fr}, in Equation (10) is affected by the surface temperature of the airside heat exchanger, ambient air temperature and relative humidity, air velocity, and frosting time. The longer the frosting time is, the greater the frost density will be.

When performing simulation, an initial density would have to be assumed, and for each time step the change of frost density and frost thickness may be determined by:

$$\Delta\rho_{fr} = (\dot{m}_\rho / A_t \delta_{fr})\Delta t \tag{11}$$

$$\Delta\delta_{fr} = (\dot{m}_\delta / A_t \rho_{fr})\Delta t \tag{12}$$

These increments are added to the values of frost density and thickness, respectively, at the previous time step in order to obtain the density and thickness at the present computing time step. The thermal conductivity of frost was evaluated by [19]

$$\lambda_{fr} = 0.001202\rho_{fr}^{0.963} \tag{13}$$

4. The heat exchanger sub-model

The heat exchanger sub-model can be divided into three modules. They are refrigerant side module, pipe wall module and airside module, respectively. The detailed descriptions of each of these modules are as follows.

4.1. Refrigerant side module

Two refrigerant flow regions exist inside airside heat exchanger coil in an ASHPWHC unit: a two-phase region and a superheat region. In the two-phase region, when the mass flow rate is high, annular flow exists if the refrigerant dryness fraction x is below 0.95. The value of x after a throttling valve is usually around 0.2, therefore, annular flow dominates in the two-phase region.

4.1.1. Two-phase region (annular flow)

Applying both the mass and energy balances yields:

$$\frac{\partial}{\partial t}[\bar{\alpha}\rho_V + (1-\bar{\alpha})\rho_L] + \frac{\partial}{\partial z}[\bar{\alpha}\rho_V u_V + (1-\bar{\alpha})\rho_L u_L] = 0 \tag{14}$$

$$\frac{\partial}{\partial t}[\bar{\alpha}\rho_V h_V + (1-\bar{\alpha})\rho_L h_L] + \frac{\partial}{\partial z}[\bar{\alpha}\rho_V u_V h_V + (1-\bar{\alpha})\rho_L u_L h_L] = \frac{4}{D_i}\dot{q}_{tp} \tag{15}$$

where

$$\dot{q}_{tp} = \alpha_{tp}(T_{PW.i} - T_e)$$

α_{tp} is the heat transfer coefficient in the two-phase region. Because of the difference of heat transfer coefficients between wet wall region ($0.2 < x < x_d$) and dry-out region ($x \geqslant x_d$), they are evaluated, respectively, by [20]

$$\alpha_{tp} = \begin{cases} \alpha_r(x) & 0 < x \leqslant x_d \\ \alpha_r(x_d) - [(x - x_d)/(1 - x_d)]^2(\alpha_r(x_d) - \alpha_S) & x > x_d \end{cases} \tag{16}$$

where

$$\alpha_r(x) = 3.4\left(\frac{1}{X_{tt}}\right)^{0.45}\alpha_L$$

$$\alpha_L = 0.023(\lambda_L/D_i)Re_L^{0.8}Pr_L^{0.3}$$

$$X_{tt} = \left(\frac{1-x}{x}\right)^{0.9}\left(\frac{\mu_L}{\mu_V}\right)^{0.1}\left(\frac{\rho_V}{\rho_L}\right)^{0.5}$$

$$x_d = 7.943[Re_V(2.03 \times 10^4 Re_V^{-0.8}(T_{PW} - T_e) - 1)]^{-0.161}$$

Applying the momentum balance and neglecting the time item because of the fast transfer of momentum yields

$$\frac{\partial}{\partial z}[\bar{\alpha}\rho_V u_V^2 + (1-\bar{\alpha})\rho_L u_L^2] = -\frac{\partial p}{\partial z} - F_{PW.L} \tag{17}$$

There are four unknown variables u_V, u_L, p, $\bar{\alpha}$ in Eqs. (13), (14) and (16). In order to solve these equations, a void faction equation must be added.

Currently, there exist four types of models for void fraction, i.e., the uniformity phase model, the modified slip ratio model, the modified X_{tt} model and the model considering mass flow rate. In this study, based on the calculation results using the current model and their comparisons with the existing results from literature [20], the modified X_{tt} model was selected from previously reported studies, i.e.,

$$\begin{cases} \bar{\alpha} = (1 + X_{tt}^{0.8})^{-0.378} & X_{tt} \leqslant 10 \\ \bar{\alpha} = 0.823 - 0.157\ln X_{tt} & X_{tt} > 10 \end{cases} \tag{18}$$

4.1.2. Superheat region

Applying both the mass conservation and energy conservation yields

$$\frac{\partial \rho_{Sp}}{\partial t} + \frac{\partial}{\partial z}(\rho_{Sp} u_{Sp}) = 0 \tag{19}$$

$$\frac{\partial}{\partial t}(\rho_{Sp} i_{Sp}) + \frac{\partial}{\partial z}(\rho_{Sp} u_{Sp} i_{Sp}) = \frac{4}{D_i}\dot{q}_{Sp} \tag{20}$$

where

$$\dot{q}_{Sp} = \alpha_{Sp}(T_{PW.i} - T_e)$$

$$\alpha_{Sp} = 0.023 Re_{Sp}^{0.8} Pr_{Sp}^{0.4} \lambda_{Sp}/D_i$$

The conservation of momentum requires

$$\frac{\partial}{\partial z}(\rho_{Sp} u_{Sp}^2) = -\frac{\partial p}{\partial z} - F_{PW.Sp} \tag{21}$$

There are three unknown variables u_S, p, T_e in Eqs. (18)–(20). Therefore, the three variables can be obtained by solving the three equations.

4.1.3. Refrigerant-side pressure drop

Superheat region. The pressure drop in the superheat region was calculated by [20]

$$\Delta p_{Sp} = f_{Sp} \frac{\rho_{Sp} u_{Sp}^2}{2D_i} \Delta z_i \tag{22}$$

where the friction coefficient f_{Sp} can be expressed as follows:

$$f_{Sp} = \begin{cases} 64/Re_{Sp} & Re_{Sp} < 2320 \\ 0.3164 Re_{Sp}^{-0.25} & 2320 \leqslant Re_{Sp} \leqslant 8 \times 10^4 \\ 0.0054 + 0.3964 Re_{Sp}^{-0.3} & Re_{Sp} > 8 \times 10^4 \end{cases} \tag{23}$$

Two-phase region. The refrigerant pressure drops in the two-phase region is considered being related to the pressure drops in both gas and liquid phase, and also to refrigerant dryness fraction [21].

$$\Delta p_{tp} = [\Delta p_L + 2(\Delta p_V - \Delta p_L)x](1-x)^{1/3} + \Delta p_V x^3 \tag{24}$$

where Δp_L and Δp_V are pressure drop for refrigerant liquid and gas, respectively.

4.2. Pipe wall module

Applying the energy conservation equation yields

$$c_{p.PW} M_{PW} \frac{\partial T_{PW}}{\partial t} = \dot{Q}_a - \dot{Q}_r \tag{25}$$

Because pipes and fins in the heat exchanger may be made of different materials, an average specific heat for pipe and fin ($c_{p.PW}$) is used as follows:

$$c_{p.PW} = \frac{c_{p.p} M_p + c_{p.f} M_f}{M_p + M_f}$$

4.3. Airside module

The mass conservation equation is

$$\frac{d(\dot{m}_a d)}{dz} = (\pi D_o)\dot{w} \tag{26}$$

The energy conservation equation is

$$\frac{d(\dot{m}_a i_a)}{dz} = (\pi D_o)\dot{q}_{a.t} \tag{27}$$

where $\dot{q}_{a.t}$ is the total heat flux on airside, and can be expressed by

$$\dot{q}_{a.t} = \frac{(A_o + \eta_f A_f)}{\pi D_o \Delta z_i} \alpha_{a.t} (h_{St} - h_a) \tag{28}$$

where h_{St} is the saturated air enthalpy at the coil surface temperature. The total heat exchange coefficient $\alpha_{a.t}$ is determined by the j factor method [22], as follows:

$$\alpha_{a.t} = \frac{\dot{m}_a j_t}{A_{min} Sc_a^{2/3}} \tag{29}$$

where

$$Sc_a = v_a/D_S$$

$$j_t = \left[\frac{1 - 1280 n Re_1^{-1.2}}{1 - 5120 Re_1^{-1.2}}\right][0.0014 + 0.2618 \times JP \times (0.95 + 4 \times 10^{-5} Re_3^{1.25})]\left(\frac{S_f}{S_f - \delta_f}\right)^2$$

$$JP = Re_2^{-0.4}\left(\frac{A_o}{A_t}\right)^{-0.15}$$

$$Re_1 = \frac{\dot{m}_a S_2}{A_{min}\mu_a}; \quad Re_2 = \frac{\dot{m}_a D_o}{A_{min}\mu_a}; \quad Re_3 = \frac{\dot{m}_a S_f}{A_{min}\mu_a}$$

The fin efficiency under frosting was adopted from literature [23]

$$\eta_f = \frac{th(m \cdot L)}{m \cdot L} \tag{30}$$

$$m = \sqrt{\frac{1}{c_{p.a}/(\alpha_{a.s} \cdot a_1) + \delta_{fr}/\lambda_{fr}} \cdot \frac{1}{\lambda_f \cdot \delta_f}} \tag{31}$$

where the fin equivalent height L was calculated by [24]:

$$L = \frac{D_o}{2}(\tau - 1)(1 + 0.35 \ln \tau)$$

$$\tau = 1.063 S_l/D_o$$

The airside pressure drop was evaluated based on Turaga [25]:

$$\Delta p_a = f \frac{(\dot{m}_a/A_{min})^2}{2\rho_a} \frac{A_t}{A_{min}} \tag{32}$$

where

$$f = 0.129\left(\frac{\dot{m}_a D_o}{A_{min}\mu_a}\right)^{-0.227}$$

Eqs. (1)–(32) form the complete distributed mathematical model for the airside heat exchanger under frosting in an ASHPWHC unit. A forward-difference technique with implicit time was employed in solving differential equations when carrying out simulation.

5. Model validation

An airside heat exchanger, with its detailed specifications shown in Table 1 and Figs. 1 and 2, has been used for carrying out simulation using the distributed model reported. The airside heat exchanger is made up of 16 refrigerant circuits as shown in Fig. 1. Each circuit consists of 10 sub-circuits. As can be seen in Figs. 1 and 2, there are four heat exchange rows in this heat exchanger. The total length of each sub-circuit, as sketched in Fig. 2, is 16 m. The heat exchanger simulated is divided into many elements along the flow direction of refrigerant, as shown in Fig. 3. The governing equations discussed above can be applied to each of these elements.

Fig. 4 presents an example of the comparisons between the simulation results using the model developed in this paper and the previous published experimental results on frost accumulation per unit heat exchanger area against operating time. The simulated operating air relative humidity was 85%, ambient air temperature 1.5 °C, refrigerant evaporation temperature −7.5 °C and wind velocity 3.3 m/s. It is seen that the simulated results using the current model agreed well with the experimental data [13], with a maximum error of 8.6% at 60 min.

Comparing the simulation results using the distributed model reported with those available in open literature for other operating parameters also suggests that the model developed is valid. For example, the trends of change in frost accumulation against time agreed well with the existing experimental data and other simulation results [8,10], and the simulated results of the frost accumulation in different row locations (totally four rows) under three different operating conditions also agreed well with the previous experimental results by others [26].

Table 1
Geometry details of the heat exchanger coil used in simulation

Item	Name	Material/number/description
1	Tube material	Copper
2	Fin material	Aluminum
3	Fin form	Ripple-fin
4	Number of tube row	4
5	Tube diameter and thickness	$\varphi 10 \times 0.5$ mm
6	Space of tube S_1	25.4 mm
7	Space of row S_2	22 mm
8	Fin pitch	2.0 mm
9	Fin coefficient	17.8
10	Fin thickness	0.2 mm
11	Single pipe length	16 m
12	Number of sub-liquid refrigerant circuit	10

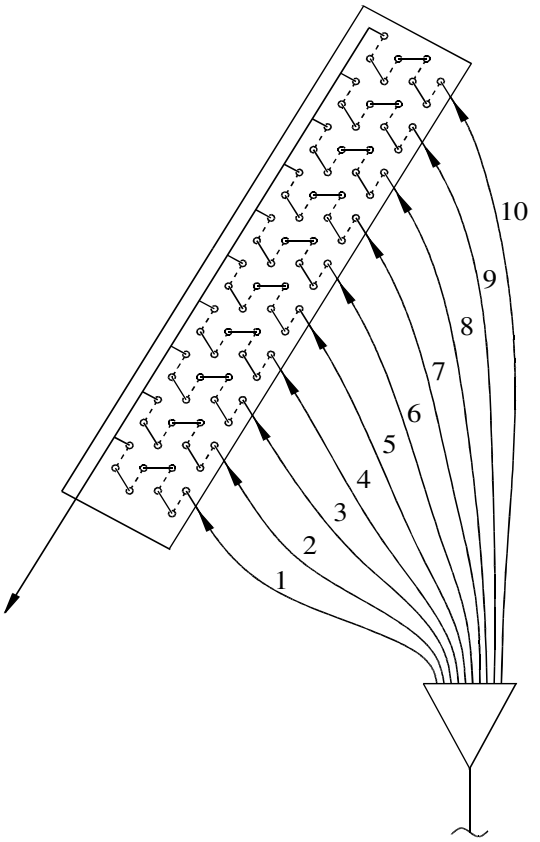

Fig. 1. A refrigerant distribution circuit containing 10 sub-circuits.

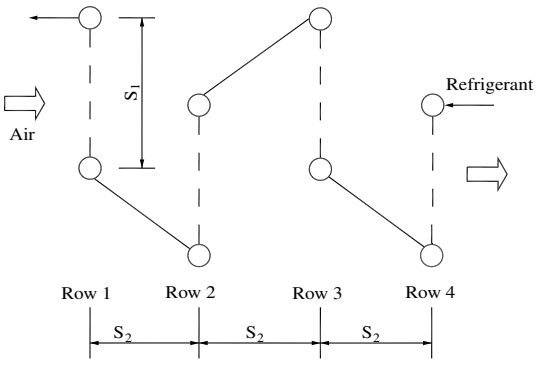

Fig. 2. Sketch of a sub-refrigerant distribution circuit.

6. Operational characteristics evaluation

The airside heat exchanger under frosting used in simulation for operational characteristics evaluation is the same as that used for model validation. The ambient or operating conditions (i.e., Conditions A–F) used in

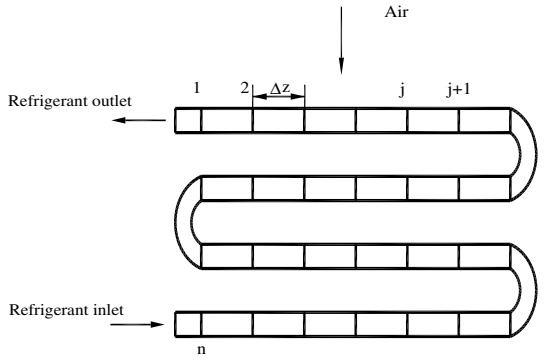

Fig. 3. Division of pipe element in the flow direction of refrigerant.

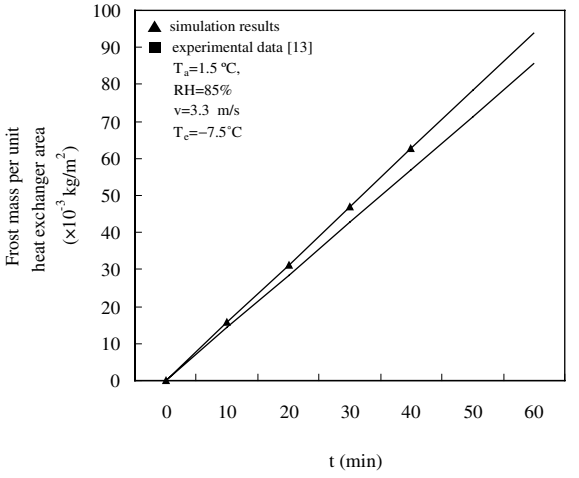

Fig. 4. Comparison between the simulation and previous experimental result of frost mass per unit area on the surface of heat exchanger vs. time.

simulations are given in Table 2. The properties of refrigerant used in simulation are from literature [1].

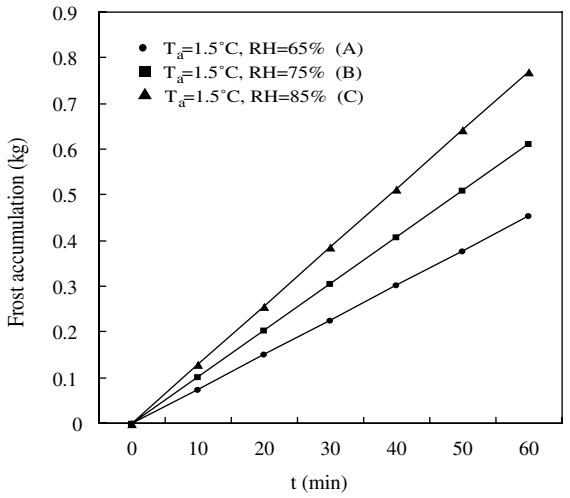

Fig. 5. Frost mass accumulation against time under different relative humidities.

Examples of simulation results for major system operational characteristics under frosting such as frost accumulation, thickness and distribution on surface of the airside heat exchanger under different ambient/operating conditions, and for the impacts of frosting on the operational performance of an ASHPWHC unit under frosting, such as the total heat transfer and airflow resistance, are presented in Figs. 5–13.

Fig. 5 presents the simulated results for frost mass accumulation against time and Fig. 6 the simulated frost thickness against time under Conditions: A–C (wind velocity 2.5 m/s), respectively. As can be seen in Fig. 5, more frost will be formed on coil surface with the increase of time; a higher air relative humidity would result in more frost accumulated. As shown in Fig. 6, the frost thickness also increases with time elapsing; the higher the air relative humidity, the faster the increase of frost thickness. These are expected, since the driving potential of mass transfer between air and cold coil surface is greater at a higher air humidity. This helps explain why an air source heat pump frosts severely at high ambient humidity when operated in heating mode.

Table 2
Ambient/operating conditions used in simulation

Condition	Ambient air temperature (°C)	Relative humidity (%)	Air flow(m^3/h)	Evaporation temperature (°C)	Degree of superheat (°C)	Condensing temperature (°C)	Degree of subcooling (°C)	Flow of refrigerant (kg/s)
A	1.5	65	1061.3	−13	5	50	5	0.0096
B	1.5	75	1061.3	−13	5	50	5	0.0096
C	1.5	85	1061.3	−13	5	50	5	0.0096
D	−4	65	1061.3	−17	5	50	5	0.00816
E	−4	75	1061.3	−17	5	50	5	0.00816
F	−4	85	1061.3	−17	5	50	5	0.00816

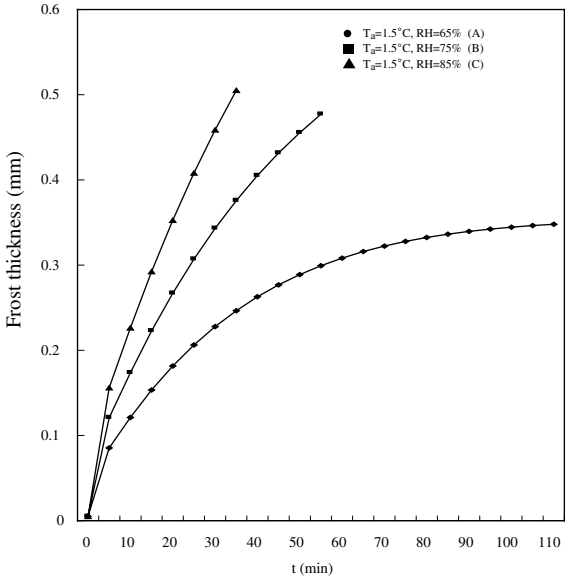

Fig. 6. Frost thickness vs. time under three different sets of relative humidity.

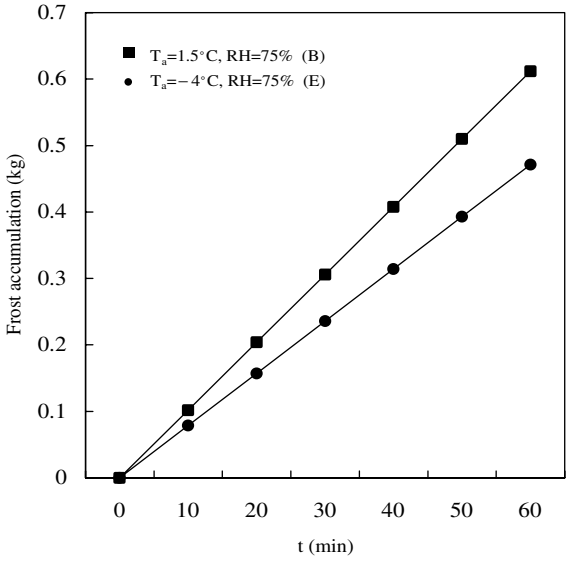

Fig. 7. Frost mass accumulation against time at two different ambient air temperatures.

The trends of change shown in Fig. 5 agree well with the existing experimental data and other simulation results [8,10]. Furthermore, it is noted from Fig. 6 that the frost thickness increases non-linearly with frosting time, fast increase at the start and gradually slowing down afterwards. This is because the density of frost at layers close to tubes gradually increases with the time, as water vapor penetrates and solidifies through these layers.

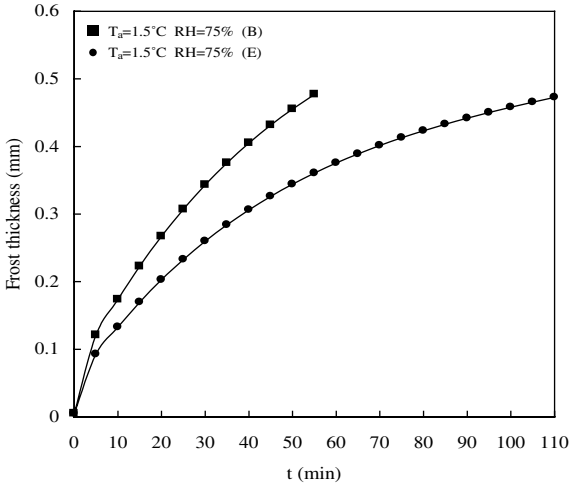

Fig. 8. Frost thickness against time at two different ambient air temperatures.

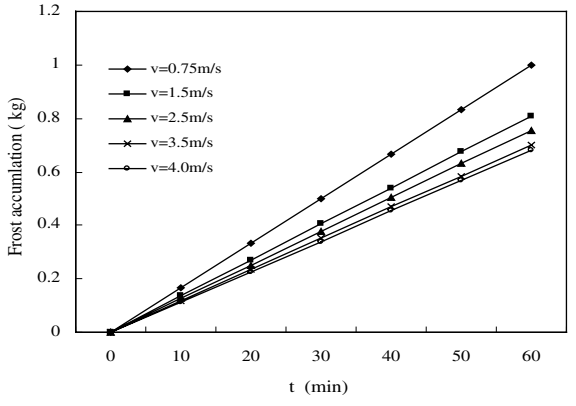

Fig. 9. Frost mass accumulation against time at different wind velocities.

Figs. 7 and 8 illustrate the simulated frost mass accumulation and frost thickness against time, respectively, under Conditions B and E. It is seen in Fig. 7 that at a higher air temperature, more frost is accumulated. Fig. 8 shows that at 1.5 °C, it takes 60 min for frost thickness to reach to 0.47 mm on heat exchanger surface. However, at −4 °C, it would take 110 min to reach the same thickness. Therefore, it may be concluded that at a constant relative humidity, the higher the ambient air temperature, the faster the increase of frost thickness. This is obvious because air with a higher temperature at a constant relative humidity contains more water vapor.

Fig. 9 depicts the effects of varying wind velocity on frost formation. At a higher wind velocity, less frost could be accumulated on coil surface, because the increase of velocity results in a decrease of frost surface

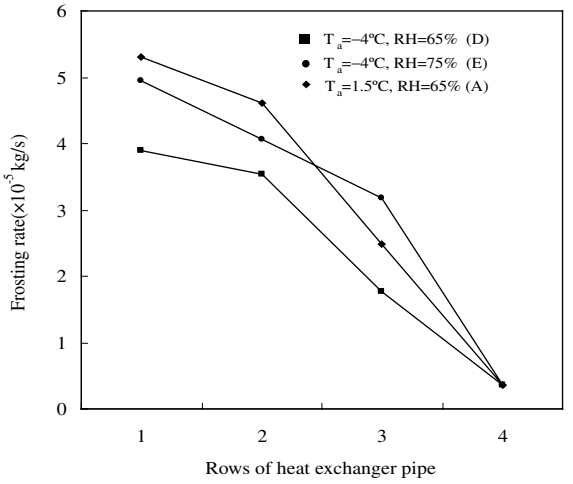

Fig. 10. Frosting rate at different rows of pipe.

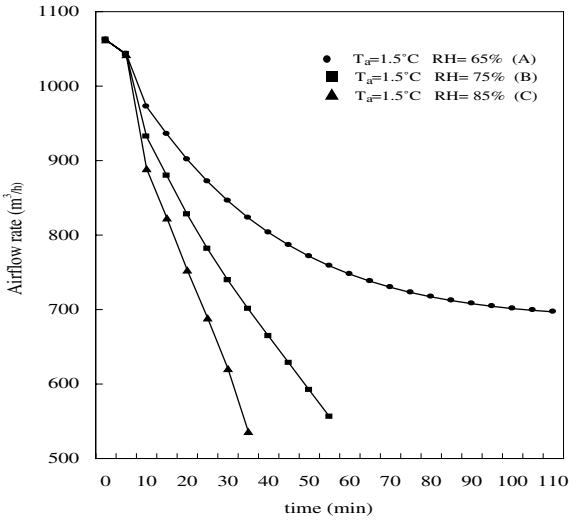

Fig. 11. Airflow rate vs. time under different relative humidities.

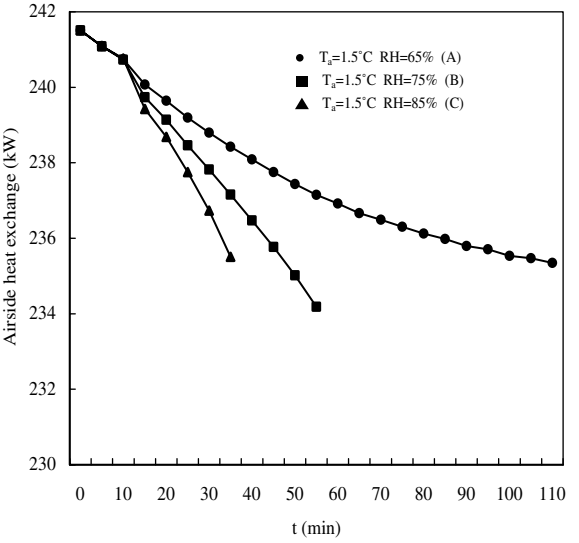

Fig. 12. Airside heat exchange vs. time under different conditions.

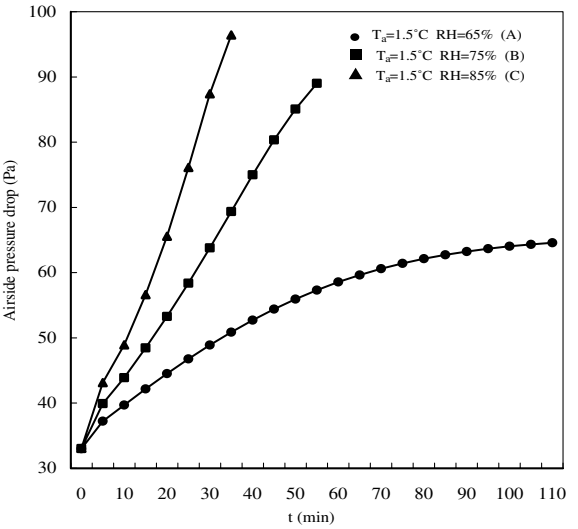

Fig. 13. Airside pressure drop vs. time under different conditions.

roughness and an increase in frost density, making the penetration of water vapor into a frost layer more difficult. This is contrary to that in free convection as described by Sami and Duong [4], but agrees with the experiment results by Yan and Li [27]. Therefore, for an ASHPWHC unit, increasing wind velocity would be a method that may be considered to delay frost formation and growth. However, this may increase the resistance to air flow.

Fig. 10 shows the frosting rate in different row locations (totally four rows) under Conditions D, E and A, respectively. Row 1 is the pipe row located nearest the wind inlet and row 2 the second, and so on. It can be seen that the nearer a tube row is relative to the wind inlet, the more the frost accumulation on it will be. Table 3 presents the simulated results of the percentage breakdown of frost accumulation on each of the four rows. It shows that the frost accumulation was mainly on the front rows of heat exchanger pipe, particularly in the first row. For example, in Condition A, the frost accumulation on the first and second row is already 77.8% of the total frost accumulation on the heat

Table 3
Percentage breakdown of frost accumulations on each of the four rows

Condition	Row			
	1 (%)	2 (%)	3 (%)	4 (%)
A	41.7	36.1	19.4	2.8
D	40.7	37.1	18.5	3.7
E	39.5	32.3	25.4	2.8

exchanger surface, of which 41.7% is on the first row. On the contrary, the frost accumulation on the back rows is relatively insignificant, 19.4% on the third and 2.8% on the fourth row, respectively. This agrees well with the previous experimental results by others [25]. Therefore, a staged fin-coil heat exchanger is considered superior to that of equivalent fin pitch coil for an ASHPWHC unit under frosting in heating mode. Also currently, the temperature sensors used for defrosting are evenly distributed over rows of an airside heat exchanger. Therefore uneven distribution of these temperature sensors, i.e., more sensors on the front rows, is suggested.

Fig. 11 presents the simulated airflow rates against time under Conditions A, B and C, respectively. The following can be observed:

- Airflow rate decreases rapidly with increased frost accumulation; the decreasing trend is strongly affected by air relative humidity.
- The higher the ambient air humidity is, the more rapidly the airflow rate decreases. For example in Condition C, when the unit was operated for 30 min, air flow is reduced from 1062 to 620 m^3/h and the net air flow reduction is 441 m^3/h which is 42% of the total airflow rate. In Condition B, the net air flow reduction of 322 m^3/h is 30% of the total airflow rate. However, in Condition A the net air flow reduction of 216 m^3/h is only 20% of the total airflow. These are considered to have been caused by different frost thicknesses under different ambient conditions, as shown in Fig. 6.

Fig. 12 shows the simulated total heat transfer of the airside heat exchanger against time under Conditions A–C, respectively. It is found that the total heat transfer will be reduced with the increase of frost thickness; the higher the relative humidity, the faster the reduction of the total heat transfer. This may be explained by the fact that a thicker frost formation on heat exchanger surface leads to a greater reduction of airflow rate and a higher heat transfer resistance, thus resulting in a greater reduction of the heat exchange coefficient, leading to a reduced total heat transfer, at a higher relative humidity.

As the time elapses, with more frost accumulated on the surface of a heat exchanger, the heat exchange coefficient may be significantly reduced, and heat transfer efficiency is severely deteriorated, so that the total heat transfer is decreased. Therefore, if the air flow rate is reduced to a certain value (e.g. 60% of the initial air flow rate), defrosting will be required. As can be seen in Fig. 10, using 60% of the initial air flow rate as a default, defrosting is required when the unit is operated for 30 min under Condition C and for 55 min under Condition B. This demonstrates that when the same ASHPWHC unit is operated in different climatic regions, the setting of defrosting interval should be varied. Clearly, the current defrosting control of using a unified time constant for units to be used in different climatic regions is not appropriate.

Fig. 13 indicates the airside pressure drop against time under Condition A–C, respectively. The following can be observed:

- Airside pressure drop increases rapidly with increasing frost accumulation. This is because that the increased frost thickness leads to a narrower fin pitch and a smaller air flow passage area and; hence, the air velocity and pressure drop greatly increase.
- The higher the air relative humidity is, the more rapidly the air pressure drop increases. It could be explained by the fact that moisture content increases with the increase of relative humidity at a constant air temperature, and therefore more frost is accumulated. For example, when the ASHPWHC unit was operated for 30 min, frost thickness is 0.46 mm in Condition C, 0.34 mm in Condition B, and 0.23 mm in Condition A. Hence, this causes different air pressure drops in the three operating conditions, i.e. 54.4, 30.7 and 15.8 Pa in Condition C, B and A, respectively.
- Under the three different conditions, the same air pressure drop will be resulted from the same thickness of frost, as shown in Fig. 6. For example, in Fig. 6, it takes 15 min for the frost thickness to reach 0.3 mm in Condition C, 24 min in Condition B, and 56 min in Condition A, respectively. On the other hand, in Fig. 13, 15 min elapsed when air pressure drop is 56.6 Pa in Condition C, 24 min in Condition B and 56 min in Condition A, respectively. This proves that frost thickness is a primary factor affecting airside pressure drop.

From the detailed analysis of the simulated results shown in Figs. 5–13, it can be observed that the defrosting methods currently used, i.e., time control in an ASHPWHC unit may have to be modified based on the simulated results of the mechanism of frost thickness increase. For example, if the defrosting time interval is set based on Condition C, then for Conditions B and A, defrosting will be started ahead of the

scheduled starting time, leading to unnecessary defrosting and a low efficiency. On the other hand, although time-temperature control is adopted in certain ASHPWHC units, the same defrosting starting time and intervals are used even they are intended for use in different climatic regions. Therefore, their actual defrosting effects would be dependent on ambient conditions such as air temperature, relative humidity, etc. It is therefore realized that only when an accurate prediction of frosting mechanism on the airside heat exchanger in ASHPWHC units is obtained, can the optimal defrosting effects be obtained.

7. Conclusions

A distributed model of the airside heat exchanger under frosting in an ASHPWHC unit has been developed and validated using previous experimental data available in open literature. The operational characteristics of the airside heat exchanger under frosting in an ASHPWHC unit and their effects on unit's performance have been investigated by using the distributed model. The following conclusions may be drawn:

- The mathematical model developed for an airside exchanger under frosting in an ASHPWHC unit is entirely distributed and, derived from mass, energy and momentum conservations, so it can be applied to various types of finned tube heat exchangers having different fin configurations.
- The frost formation/growth varies with ambient conditions. At a constant air temperature, the higher the air relative humidity, the more serious the frost formation, and the shorter the defrosting interval. At a constant air relative humidity, the frost formation is more serious at a high temperature than that at a low temperature when operated in heating mode below a certain air temperature above which frosting may not occur.
- With the increase of frost accumulation, the total airside heat transfer and airflow rate will decrease, and air flow resistance increases. The optimal defrosting time interval is evaluated, which is firstly seen in open literature.
- The nearer the tube row is relative to the wind inlet, the more the frost accumulation on it will be, i.e., frost accumulation is mainly on the front rows of heat exchanger pipe, particularly in the first row.

All these are expected to be useful in helping optimize the structural layout and improve defrosting measures of an airside heat exchanger under frosting in ASHPWHC units, thus, increasing its energy efficiency and operating reliability.

Acknowledgements

This project was financially supported by the National Natural Science Foundation of China (Grant no. 50278021) and China Postdoctoral Science Foundation (Grant no. LRB000145).

References

[1] Y. Yao, Simulation and analysis for air source heat pump water heater/chiller under frosting. Ph.D Dissertation, Harbin Institute of Technology, China, 2002.
[2] B.W. Jones, J.D. Parker, Frost formation with varying environmental parameters, J. Heat Transfer 97 (2) (1975) 255–259.
[3] B.T. Marinyuk, Heat and mass transfer under frosting conditions, Int. J. Refrig. 3 (6) (1980) 366–368.
[4] S.M. Sami, T. Duong, Mass and heat transfer during frost growth, ASHRAE Trans. 95 (1) (1989) 158–164.
[5] M.M. Chen, W. Rohsenow, Heat, mass and momentum transfer inside frosted tubes—experiment and theory, J. Heat Transfer 3 (9) (1964) 334–340.
[6] K.O. Beatty, E.B. Finch, E.M. Schoenborn, Heat transfer from humid air to metal under frosting conditions, J. Am. Soc. Refrig. Eng. 59 (1951) 1203–1207.
[7] C.J. Cremers, V.K. Mehra, Frost formation on vertical cylinders in free convention. ASME Paper No.80-WA/HT-22, American Society of Mechanical Engineers, New York.
[8] Y.B. Lee, S.T. Ro, An experimental study of frost formation on a horizontal cylinder under cross flow, Int. J. Refrig. 24 (2001) 468–474.
[9] Y.X. Tao, R.W. Besant, Rezkallah, A mathematical model for predicting the densification and growth of frost on a flat plate, Int. J. Heat Mass Transfer 36 (1993) 353–363.
[10] K.S. Lee, W.S. Kim, T.H. Lee, A one-dimensional model for formation on a cold flat surface, Int. J. Heat Mass Transfer 40 (1997) 4359–4365.
[11] R. Yun, Y. Kim, M.K. Min, Modeling of frost growth and frost properties with airflow over a flat plate, Int. J. Refrig. 25 (2002) 362–371.
[12] S.N. Kondepudi, D.L. O'Neal, The effect of frost growth on extend surface heat exchanger performance: a review, ASHRAE Trans. 93 (2) (1987) 258–273.
[13] T. Senshu, H. Yasuda, Heat pump performance under frosting conditions: Part I—heat and mass transfer on cross-finned tube heat exchangers under frosting conditions, ASHRAE Trans. 96 (1) (1990) 324–329.
[14] T. Senshu, H. Yasuda, Heat pump performance under frosting conditions: Part II—simulation of heat pump cycle characteristic under frosting conditions, ASHRAE Trans. 96 (1) (1990) 330–336.
[15] S.P. Oskarsson, K.I. Krakow, Evaporator models for operation with dry, wet and frosted finned surfaces: Part I—heat transfer and fluid flow theory, ASHRAE Trans. 96 (1) (1990) 373–379.
[16] S.P. Oskarsson, K.I. Krakow, Evaporator models for operation with dry, wet and frosted finned surfaces: Part II—evaporator models and verification, ASHRAE Trans. 96 (1) (1990) 381–391.

[17] S.N. Kondepudi, D.L. O'Neal, Performance of finned-tube heat exchangers under frosting conditions: Part I—simulation model, Int. J. Refrig. 16 (3) (1993) 175–180.
[18] E.R. Eckert, R.M. Drake, Analysis of Heat and Mass Transfer, McGraw-Hill, New York, 1972.
[19] C.T. Sanders, The influence of frost formation and defrosting on the performance of air coolers. Ph.D. Dissertation of Delf University, Netherlands, 1974.
[20] H. Wang, S. Touber, Distributed and non-steady-state modeling of an air cooler, Int. J. Refrig. 14 (2) (1991) 98–111.
[21] Y.T. Ge, System. Simulation study of air conditioner unit. Ph.D. Dissertation of Tsinghua University, 1997.
[22] F.C. McQuiston, Finned tube heat exchangers: state of the art for the air side, ASHRAE Trans. 87 (1) (1981) 1077–1085.
[23] S.N. Kondepudi, D.L. O'Neal, A simplified model of pin fin heat exchangers under frosting conditions, ASHRAE Trans. 99 (1) (1993) 754–761.
[24] M.A. Madi, R.A. Johns, M.R. Heikal, Performance characteristics correlation for round tube and plate finned heat exchangers, Int. J. Refrig. 21 (7) (1998) 507–517.
[25] M. Turaga, P. Lin, P.P. Fazio, Correlations for heat transfer and pressure drop factors for direct expansion air cooling and dehumidifying coils, ASHRAE Trans. 94 (2) (1988) 616–630.
[26] R.J. Watters, D.L. O'Neal, J.X. Yang, Effects of fin staging on frost/defrost performance of a two-row heat pump evaporator at standard test conditions, ASHRAE Trans. 107 (2) (2001) 240–249.
[27] W.M. Yan, H.Y. Li, Performance of finned tube heat exchangers operating under frosting conditions, Int. J. Heat Mass Transfer (46) (2003) 871–877.